Applied Energy 205 (2017) 1478–1494

Contents lists available at ScienceDirect

Applied Energy

journal homepage: www.elsevier.com/locate/apenergy

Hybrid PEMFC-supercapacitor system: Modeling and energy management in energetic macroscopic representation

Guadalupe Lopez Lopez[a,*], Ricardo Schacht Rodriguez[a], Victor M. Alvarado[a], J.F. Gomez-Aguilar[b], Juan E. Mota[a], Cinda Sandoval[a]

[a] TecNM, CENIDET, Int. Internado Palmira S/N, Col. Palmira, 62490 Cuernavaca, Morelos, Mexico
[b] CONACYT-TecNM, CENIDET, Int. Internado Palmira S/N, Col. Palmira, 62490 Cuernavaca, Morelos, Mexico

HIGHLIGHTS

- Dynamic modeling of PEMFC with temperature and air flow dependent parameters.
- Source modeling validation with experimental modules: BAHIA PEMFC and Maxwell SC.
- Integral simulation of hybrid system with simple energy flow representations.
- Energy management improves efficiency, SC SOC and decrease undesired transients.
- Energy management with cutoff frequency selection criteria and influence analysis.

ARTICLE INFO

Keywords:
PEMFC
Supercapacitor
Hybrid system
Energetic macroscopic representation

ABSTRACT

In this paper, we propose the dynamic simulation of a hybrid generator that integrates a fuel cell as the main source and a supercapacitor as the secondary source. We interface the proposed generator to the load using elementary power-conditioning units, and it is connected to a 36 V bus for DC applications. The powertrain simulator builds on the energetic macroscopic representation (EMR), and incorporates models deduced from measurements on a *Bahia* proton exchange membrane fuel cell (PEMFC) and a *Maxwell®* supercapacitor bank. A semi-empirical electrochemical model predicts the steady-state PEMFC behavior, and circuit-equivalent models estimate the dynamics of the sources. We apply a rule-based power management system, where a low-pass filter splits the power between the sources, and an EMR controller block based on the inverse-model regulates the bus voltage. We focus on the trade-off between simplicity and phenomenological PEMFC considerations, which enable us to predict PEMFC electric dynamics, and we analyze the benefits of the energy management with respect to the oxygen-starvation prevention and reduction of startups and shutdowns. We evaluate the power distribution control under vehicular solicitations at a reduced scale of 1 kW, and then under a pulsed current train. We discuss the influence of the cutoff frequency value. The results prove the efficacy with which it reduces abrupt changes in the fuel cell, and demonstrates that this source will deliver until it reaches 80% of the required power.

1. Introduction

Recent trends in the field of proton exchange membrane fuel cells (PEMFCs) include the hybridization of electric power-supply systems for stationary and portable applications. The integration of batteries, supercapacitors, or a combination of both into the powertrain enables the fulfillment of the electric energy requirements because high-energy sources and high-power sources are combined to track load variations, while the fuel cell can be operated within optimal operating limits. Hence, the introduction of secondary sources has the advantage of improving the PEMFC performance and extending its lifetime. However, in order to realize efficient operating conditions, proper control is required at different levels.

A PEMFC is an electrochemical device with a mass, momentum, and energy-transport phenomena that occurs along with electrochemical reactions through gas channels and within the membrane-electrode assembly (MEA). Wu et al. [1] reported a review of modeling studies of PEMFCs, and presented a rigorous model governing their behaviors,

* Corresponding author.
E-mail address: guadalupe@cenidet.edu.mx (G. Lopez Lopez).

http://dx.doi.org/10.1016/j.apenergy.2017.08.063
Received 3 November 2016; Received in revised form 17 May 2017; Accepted 11 August 2017
Available online 21 August 2017

which include mass, momentum, and energy-conservation equations, as well as the species transport and charge equations. A complete assessment of the fuel cell behavior can be conducted for highly complex models; however, attempts must be made to reflect the basic PEMFC static and transient performance in hybridization strategies.

From a more general point of view, the design and simulation of a complete hybrid system are also faced with the challenge of integrating elements with different dynamic time responses and important interactions, which results in computationally expensive efforts. Therefore, in order to develop hybrid systems simulators, it is important to formulate and couple dynamic models of the sources and the auxiliary equipment for plant balance and power conditioning units. A trade-off between the simplicity and comprehensive phenomenological considerations is required. With respect to the various strategies adopted for energy management in hybrid generators, current studies deal with the design of configurations and topologies for connecting different sources with power-conversion units and with the load [2–5]. To administer the energy in these systems, rule-based strategies are most commonly encountered, and some schemes are improved using fuzzy rules or either offline or online optimization algorithms [3]. Furthermore, the control structure of a hybrid power-generation system addresses a number of control objectives at different levels, and it largely determines the effectiveness of the energy-delivery completion and adequacy. The PEMFC control loops deal with the hydrogen and oxygen supply problem as well as with the humidity and temperature-management requirements. The power conditioning units typically involve a twofold control, including an inner current control and an external voltage regulation in accordance with the bus requirements. However, the power splitting is usually the main control objective [6–10]. In addition, there is an increased interest in considering the static and transient performance of the fuel cell to guarantee its operation at safe power limits, and to estimate and regulate the state of charge (SOC) of the accumulators [11,1,12–17].

Therefore, there is a need to review studies in order to provide a comprehensive analysis of the PEMFC behavior, and the following works are good examples: [18–20]. A significant issue is that experimental systems exhibit characteristic transient phenomena, which either occur with load variations, or which are due to predictable or unpredictable changes of pressure, temperature, humidity, and gas flow; therefore, the double-layer capacitance effect determines the voltage evolution during step-down transients, while the overshoot and the undershoot phenomena produce additional positive or negative voltage variations during rapid fluctuations in load [20], while the reversal of the polarity causes voltage drops during the process of the reactants starvation episodes of distinct origins [21,22].

It is known that renewable-energy sources are distinguished by their continuous startups and shutdowns, as well as their variability and intermittency. Therefore, the above-described transients are recurrent and can lead to failure modes, performance degradation, corrosion problems, and aging acceleration in PEMFCs. These characteristic operating features entail wide-ranging conditions in the fuel cell, and transient phenomena may have different origins. In particular, the undershoot phenomenon is caused by sudden hydrogen and air starvation. In turn, oxygen starvation is attributed to an insufficient oxygen supply, non-uniform oxygen distribution, the prevalence of a pressure difference between the anode and cathode, cathode flooding or drying, an increased stack temperature, and deficient gas reactions [1,18]. On the other hand, hydrogen starvation is attributed mainly to the drying of the membrane caused by changes in the water electro-osmotic drag [23].

PEMFC hybrid systems are clearly multi-physical; thus, energy-flow models are potentially useful to obtain straightforward graphical structures that represent their performance. For example, the bond graphs model and the energetic macroscopic representation (EMR) use causal graphic descriptions to represent the conversions and exchange of energy that takes place in multi-energy domain systems. The EMR is based on the causal ordering graph (COG); here, the integral causality is mandatory [24]. The EMR includes basic coupling elements that represent the multi-energy components of a system, and includes control elements that allow the deduction of inversed-model based control loops. The formalism of this energy-flow modeling methodology was presented in [25]. The EMR was originally conceived to provide a systematic description of electromechanical systems, but it was soon extended to describe other types of conversion systems comprising the control design for diverse applications and the development of the simulation tool Portunus [26–29].

Some studies of PEMFC modeling and control using the EMR approach include [30–34]. In these works, the proposed PEMFC models predict the electric, fluidic, and/or thermic dynamics, and they introduce inversion-based control loops; moreover, these studies include the analysis and modeling of auxiliary elements, e.g., water-management or fuel-processing units. In a similar study, Agbli et al. [35] proposed an EMR of a PEM electrolyzer, and highlighted the characteristics in terms of the readability, modularity, and functionality of the model to include the electrochemical, thermodynamical, thermal, and fluidic phenomena that occur in the system.

Based on the knowledge of the transient phenomena origins, and with the aim of overcoming the drawbacks imposed by the slow response of fuel cells and by the typical fluctuating associated loads, the encountered proposals include the control objectives of strategies that are adopted for energy management in hybrid generators, which were previously presented. Other proposals that considering fuel cells as a single source also focus on improving the system design and sizing [17,36], incorporating steady-state and dynamic optimization [17], or emphasizing the development of control schemes [37,38], including the regulation of the water, temperature, and flow-management subsystems.

The multiphysics nature of the EMR simplifies the simulation of hybrid PEMFC-based power-generation systems. Boulon et al. [39] proposed an EMR for a PEMFC-supercapacitor system, and included a simple energy distribution strategy. In a second work [40], they analyzed the interaction with other sources. A further study of hybrid systems involved the application of a new strategy considering the systems limits to include the saturation management of a hybrid PEMFC-ultracapacitor power source [41]. Considering the same control purpose, Castaings et al. [42] analyzed real-time energy management strategies for battery-supercapacitor hybrid sources in vehicular applications. They compared two management strategies: an optimization-based strategy that involves minimizing a performance-constrained criterion, and a rule-based strategy that uses a low-pass filter to split the current between high- and low-frequency dynamics. Results of the study revealed that both strategies have equivalent performances for real driving requirements, and they emphasized the EMR highlights to represent all of the elements of the systems and to deduce control strategies. Other studies that focus on the energy management are reported in [43,44]. Supplementary investigations that focused on the simulation and control of electric vehicles or hybrid electric vehicles considering EMRs include those by [45,31,46,47].

Thus, hybrid-generation schemes may have different degrees of complexity. As previously explained, energy-management strategies cover several operational objectives, but the dynamic fuel cell representations that are used for those purposes rarely capture overshoot, undershoot or reverse voltage. Consequently, the advantages of achieving energy management cannot be realized vis-à-vis the prevention of failure, degradation, and lifetime shortening, even if we use well-conditioned and structured rules and controllers. Different types of investigations attempt to capture electrical dynamics or starvation causes by performing a thorough assessment and modeling of the fuel cell phenomena; however, there is no interest on examining the model within a complete generator system (e.g., [48–50]).

The main goal of this paper is to provide appropriate and straightforward dynamic models of fuel cell and supercapacitor devices, which

are useful for incorporation into a hybrid powertrain simulator containing fundamental components and control loops. We estimated the parameters of the models from measurements obtained using a 1200 W *Bahia* PEMFC module constructed by *HELION*, as well as measurements obtained from a 400 F, 16 V *Maxwell* supercapacitor bank. We designed a general energy-management control system to complete the system simulator. We built the multi-physics system simulator a energetic macroscopic representation (EMR) platform containing inverse-model based control elements that facilitate the local and global control integration. The energy distribution approach uses the frequency analysis of the fuel-cell signals, and is proven in the built simulation environment under scaled powertrains that represent standard city driving conditions as well as pulse current trains to characterize fluctuating loads.

The highlight of this work is the formulation of a simple empirical dynamic circuit model of a PEMFC with the following features:

1. Contrary to the classical circuit models with constant parameters, the proposed model has temperature- and flow-dependent parameters to capture electric transients that match experimental data obtained by the PEMFC module. The model essentially predicts the double-layer capacitance effect as a function of the operating temperature and the undershoot phenomenon as a function of the oxygen flow.
2. The simplicity of the model enables us to simulate a hybrid generator including basic components of the system and an energy-management strategy with straightforward rules to achieve control objectives.
3. The model enables us to evaluate the energy management in terms of the SC SOC and the PEMFC low-heating value (LHV) efficiency estimations, as well as in terms of the startup and shutdown smoothing, the undershoot prevention efficacy, and the oxygen consumption reduction.
4. The issues pertaining to the simulator are well-suited for scaled vehicular applications and for turning-on/turning-off connected appliances.

2. Material and methods

The experimental data presented in this paper were obtained from two systems: A *Bahia* PEMFC power module and a Maxwell supercapacitor bank. The *Bahia* power module is an industrial didactic bench composed of a stack of 24 PEM monocells, and it generates a voltage ranging from 14 to 22 V, and provides a maximum current of 75 A; the module incorporates reactants supply manifolds using an air humidifier and a water circuit to control the operating stack temperature (Fig. 1). The module has three circuits: a hydrogen circuit, oxygen circuit, and a cooling water circuit (Fig. 2).

In the first circuit, the hydrogen enters in dead-end mode on the anode side from a storage tank with pressure regulation and furnished with a pressure sensor PT400.

The air enters in circulating mode on the cathode side. The stoichiometry of oxygen can be selected from within a range of 1.5–2.5. We performed all of the experiments using a stoichiometric oxygen excess ratio that is equal to 1.5. In the second circuit, the oxygen is obtained from the air provided by a lateral channel blower; the air passes through a membrane humidifier before being fed to the fuel-cell stack. The non-reacted humidified air leaving the fuel cell stack is reutilized in the humidifier, after which it is released into the atmosphere. We carried out the experiments at a relative humidity of 80%.

In the third circuit, the water is utilized in a cooling circuit to mitigate the heat of the exothermic reactions. The cooling circuit has a temperature controller that is always in operation. The temperature was then regulated at a value reference of 65 °C.

The *Maxwell* supercapacitor bank MOD0500 P016 B01 is composed of six supercapacitors connected in series (Fig. 3); the module

Fig. 1. Experimental Bahia system.

specifications are summarized in Table 1. We performed experiments in order to register the supercapacitor behavior during the delivery and recovery cycles. The data was registered at constant current values within the range of 5–40 A, with increments of 5*A*. The current was measured using a Hall effect sensor that provides 5 V/50 A. The measurements were treated using a data acquisition system (National Instruments, model USB-9211A). An elektro-automatik DC source, model EA-PS 8080-120, supplies energy to charge the supercapacitor, and an EA elektro-automatik electronic load, model EA-EL 9080-200, recovers energy from the supercapacitor to emulate the discharge cycle.

3. Integrated simulator of a 1 kW hybrid generation system

3.1. PEMFC modeling

We predicted the steady-state behavior of the fuel cell using a pseudo-empirical electrochemical model. Then, we combined it with an equivalent circuit (EC) to describe the electric dynamics of the PEMFC. Finally, we obtained the EMR from these models. The proposed PEMFC models are based on the experimental work of Zamora and Escobedo [51]. We adjusted the parameters of the polarization-curve model to ensure consistency with the power level of the experimental fuel-cell module. The proposed EC reproduces the dynamics that are due to the double-layer capacitance effect and the undershoot phenomenon. We used data from the *Bahia* PEMFC module to adjust the model parameters.

In practice and for the sake of security, the fuel cell operates out of the concentration region; consequently, we considered only the activation and Ohmic overpotentials in the cathode to predict the polarization curves. The resulting steady-state model is the semi-empirical set of Eqs. (1)–(8)

$$V_{fc} = (E - \eta_{act} - \eta_{Ohm}) N_{cell} \tag{1}$$

$$E = 1.23 - 8.456 \times 10^{-4}(T_{fc} - 298.15) + 4.308 \times 10^{-5} T_{fc} (\ln(p_{H_2}) + 0.5\ln(p_{O_2})) \tag{2}$$

$$j = \frac{I_{fc}}{A_{mc}} \tag{3}$$

$$\eta_{act} = \frac{2.3R\,T_{fc}}{\alpha(T_{fc}) z F} \ln\left(\frac{j + j_n}{j_o(T_{fc})}\right) \tag{4}$$

$$\eta_{Ohm} = (j + j_n) R_m(T_{fc}) \tag{5}$$

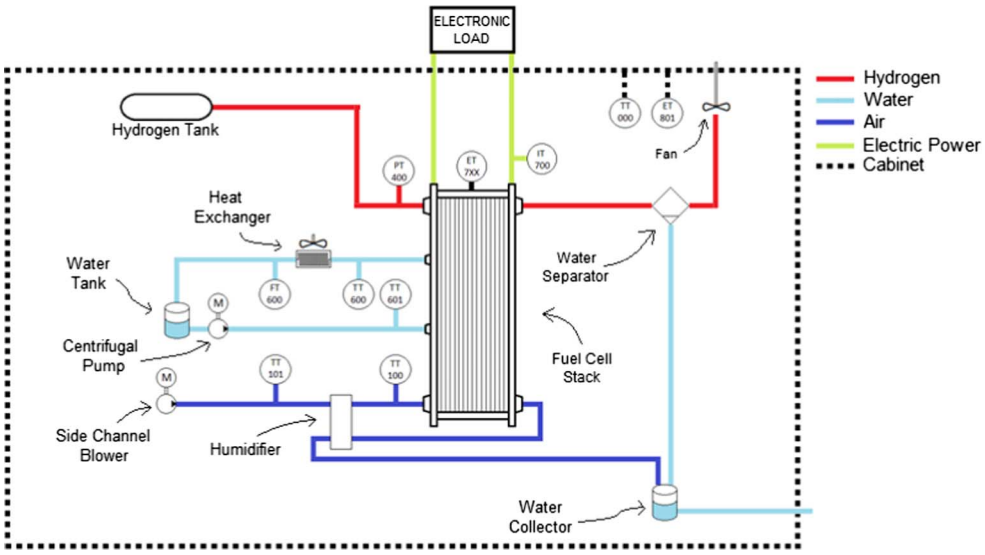

Fig. 2. Bahia system diagram.

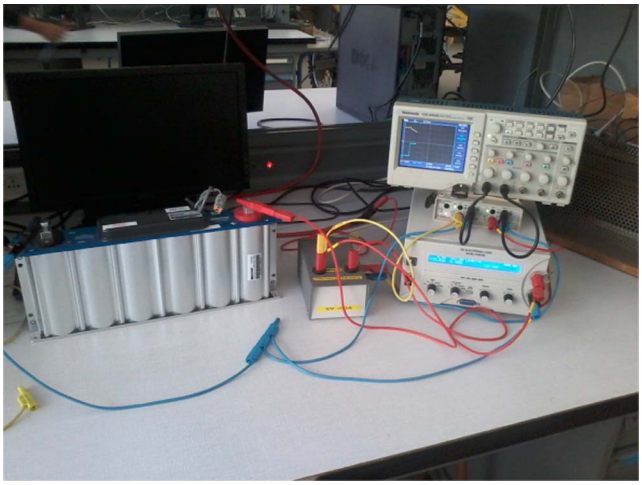

Fig. 3. Experimental Maxwell supercapacitor bank.

Table 1
Supercapacitor parameters.

Rated capacitance	500 F
Minimum capacitance, initial	500 F
Maximum capacitance, initial	600 F
Maximum ESR_{DC}, initial	2.1 mΩ
Test current for capacitance and ESR_{DC}	100 A
Rated voltage	16
Minimum operating temperature	−40 °C
Maximum operating temperature	65 °C

where V_{fc} is the output steady-state PEMFC voltage. The input variable is the current density j, defined in Eq. (3), where A_{mc} represents the active surface of a mono-cell and I_{fc} is the fuel-cell current. The addition of a constant current density j_n serves to correct the current density delivered by the fuel cell if a supplementary voltage drop is associated with internal currents or fuel crossover. N_{cell} is the number of cells that comprise the stack. E is the theoretical thermodynamic potential, and η_{act} and η_{Ohm} are the activation and Ohmic overpotentials, respectively. The steady-state output voltage is explicitly dependent on the fuel-cell temperature T_{fc}, as well as the hydrogen and oxygen partial pressures, p_{H_2} and p_{O_2}, respectively.

The characteristic parameters of η_{act} are the charge-transfer coefficient α and the current exchange j_0. The characteristic parameter of η_{Ohm} is the membrane resistance R_m, and it is calculated in terms of the membrane or protonic conductivity σ_m, the membrane thickness l, and A_{mc}. The electronic resistance is expected to be significantly smaller compared with the membrane resistance; thus, we considered only the membrane resistance R_m. The parameters of the model are expressed in terms of the fuel-cell operating temperature T_{fc}, as indicated in Eqs. (6)–(8).

$$\alpha(T_{fc}) = 4.141 \times 10^{-5} T_{fc}^{1.642} \tag{6}$$

$$j_o(T_{fc}) = 2.752 \times 10^{-5} \exp(2.863 \times 10^{-3} T_{fc}) \tag{7}$$

$$R_m(T_{fc}) = \frac{\rho_m(T_{fc}) l}{A_{mc}} \tag{8}$$

with:

$$\rho_m(T_{fc}) = \frac{1}{\sigma_m(T_{fc})}$$

$$\sigma_m(T_{fc}) = 1.65 \times 10^{-3} \exp(5.5 \times 10^{-3} T_{fc})$$

To complete the PEMFC model, an EC predicts the electric dynamics owing to the well-known phenomena of the double-layer capacitance and voltage undershoot. The first phenomenon corresponds to the capacitive behavior of the fuel cell, which arises from the charge accumulation between the catalytic layer and the electrolyte within the membrane-electrode assembly (MEA); the resulting transients exhibit first-order responses curves. On the other hand, sudden load changes significantly modify the oxygen demand, and voltage drops were therefore observed in the *Bahia* module output signals, indicating the presence of an undershoot phenomenon during the course of step-up transients, whereas overshoots were not observed during the course of step-down transients. The oxygen flow requirement significantly exceeds the available oxygen in the fuel cell; as a result, oxygen starvation occurs and a shoot of the fuel-cell voltage takes place. Fig. 4 exhibits the described transient phenomena that occurs during the operation of the *Bahia* module (blue[1] line) under load changes (green dashed line).

The proposed EC model (Fig. 5) has dynamic and static elements, and the double-layer capacitance effect is reproduced with the response of a capacitor element characterized by C_{dl}. It is connected in parallel with a resistance R_d, which is associated with the activation overpotential, η_{act}. The behavior of the voltage undershoot is reproduced

[1] For interpretation of color in Figs. 4, 25 and 27, the reader is referred to the web version of this article.

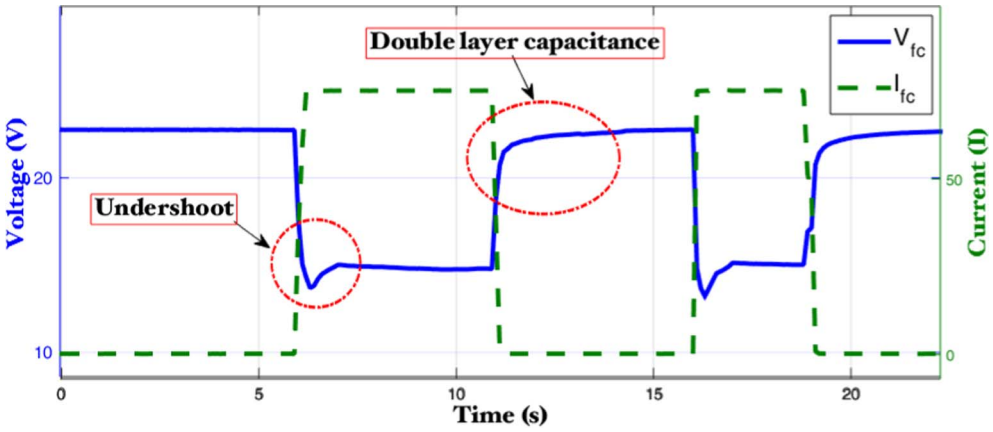

Fig. 4. Experimental electrical dynamic response of the *Bahia* system.

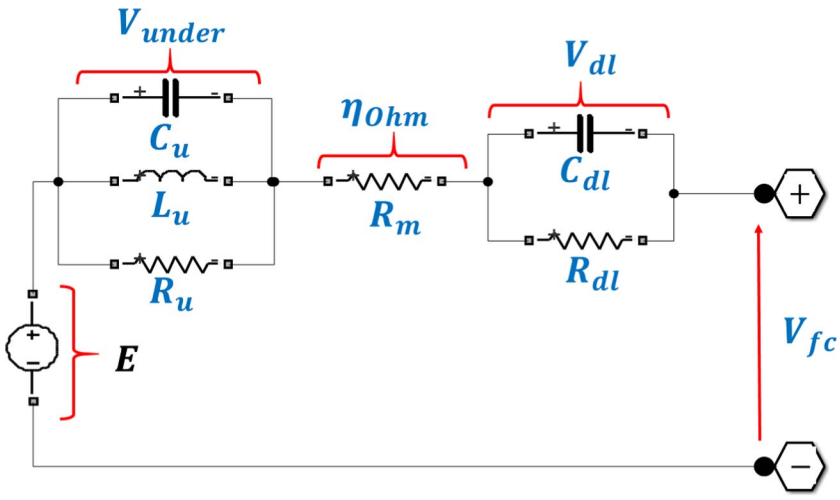

Fig. 5. Proposed dynamic equivalent circuit model of the Bahia system.

using the response of a parallel arrangement of two dynamic elements, an inductor L_u and a capacitor C_u; they are connected in parallel with their associated resistance R_u. The behavior of the undershoot inductance element is analogous to the transient behavior owing to the fluid flow that passes through a pipe in a fluidic system with an accumulation of kinetic energy. In combination with an undershoot capacitor, these elements characterize the dynamic voltage drop that is due to the oxygen starvation under abrupt load changes. The resistance R_m is the membrane resistance defined in Eq. (8), and characterizes the Ohmic overpotential defined in Eq. (5).

Contrary to the conventional EC models, the output PEMFC voltage depends explicitly on the operating variables, the parameters defining the dynamic voltage owing to the double-layer capacitance, and the PEMFC overpotentials depend on the operating temperature T_{fc}, whereas the undershoot phenomena is characterized by parameters that are dependent on the oxygen flow F_l.

The resulting dynamic model is the EC described in Eqs. (9)–(11). We computed the output fuel-cell dynamic voltage V_{fc} from Eq. (9), V_{dl} is the voltage variation due to the double-layer capacitance effect, V_{under} is the undershoot voltage, and η_{act} and η_{Ohm} are defined in Eqs. (4) and (5), respectively.

$$V_{fc} = E - V_{dl} - V_{under} - \eta_{\mathrm{Ohm}} \tag{9}$$

$$\frac{dV_{under}}{dt} = \left(-\frac{1}{L_u(W_{O_2in})C_u(W_{O_2in})} j - \frac{1}{R_u C_u(W_{O_2in})} V_{under} + j \right) \frac{1}{C_u(W_{O_2in})} \tag{10}$$

$$\frac{dV_{dl}}{dt} = \frac{1}{C_{dl}(T_{fc})} j - \frac{1}{R_d(T_{fc})C_{dl}(T_{fc})} V_{dl} \tag{11}$$

The parameters characterizing V_{dl} and V_{under} are computed with Eqs. (12) and (13), respectively.

$$\begin{cases} C_{dl}(T_{fc}) = 14.71\, T_{fc}^{-1.358} \\ R_d(T_{fc}) = \frac{\eta_{act}(T_{fc})}{j} \end{cases} \tag{12}$$

$$\begin{cases} C_u(W_{O_2in}) = 0.3\log(W_{O_2in}) + 1 \times 10^{-15} \\ L_u(W_{O_2in}) = 0.007\log(W_{O_2in}) + 2 \times 10^{-17} \\ R_u = 0.1177 \end{cases} \tag{13}$$

The oxygen pressure p_{O_2} and the hydrogen pressure p_{H_2} are determined from the mass balances Eqs. (14), (15), according to the flow model reported by [52].

$$\frac{dp_{O_2}}{dt} = \frac{R\,T_{fc}}{V_{Ca}}(W_{O_2in} - W_{O_2react}) \tag{14}$$

$$\frac{dp_{H_2}}{dt} = \frac{R\,T_{fc}}{V_{An}}(W_{H_2in} - W_{H_2react}) \tag{15}$$

where R [J K^{-1} mol^{-1}] is the ideal gas constant, and V_{Ca} and V_{An} are the volume of the cathode and the anode, respectively. We calculated the oxygen flow as indicated in Eq. (16), where λ is the stoichiometric oxygen excess ratio Eq. (17), P_{fc} is the fuel-cell power, and V_c is a monocell voltage.

$$\begin{cases} W_{O_2in} = \left(18.2 \times 10^{-3}\, \lambda\, \frac{P_{fc}}{V_c}\right) \\ W_{O_2react} = \left(4.2 \times 10^{-3} \frac{P_{fc}}{V_c}\right) \end{cases} \tag{16}$$

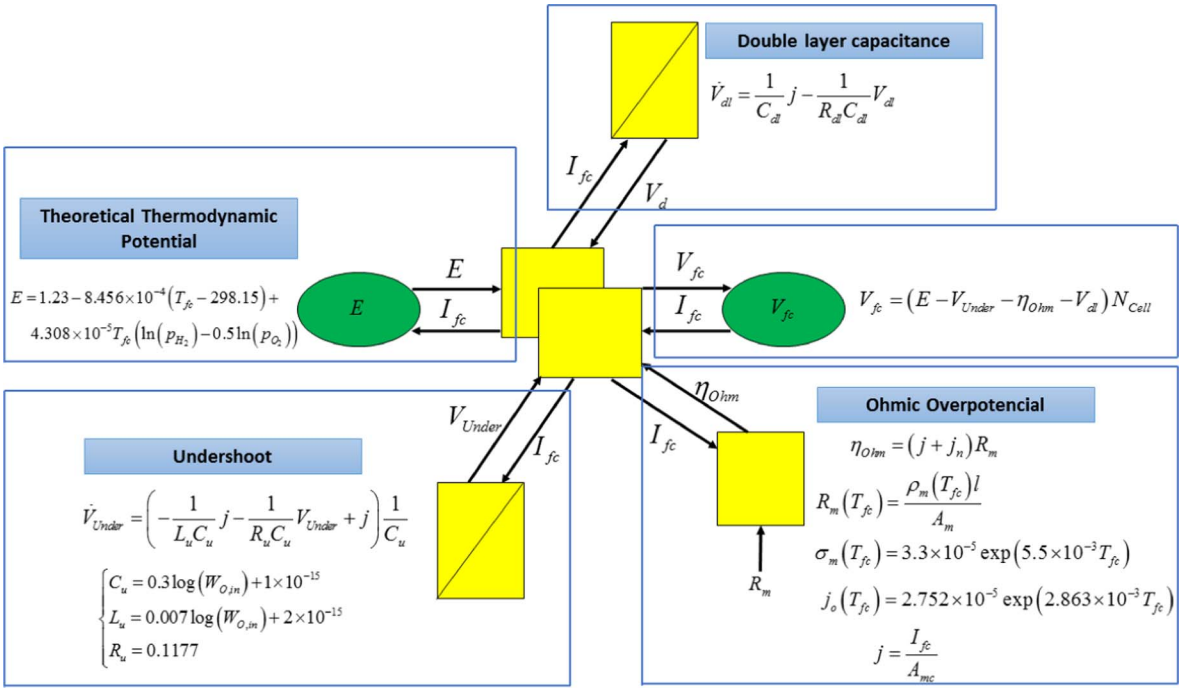

Fig. 6. EMR of the PEMFC.

$$\lambda = \frac{W_{O_2 in}}{W_{O_2 react}} \tag{17}$$

The hydrogen flow is calculated as indicated in Eq. (18)

$$W_{H_2 in} = W_{H_2 react} = \left(5.350 \times 10^{-4} \frac{P_{fc}}{V_c}\right) \tag{18}$$

We built the graphical structure of an EMR using basic elements defined in the former works of [25,47].

The EMR of the PEMFC was built from the EC model of Fig. 5, using the following components: Two accumulation elements characterize V_{dl} and V_{under}, a source represents the thermodynamic potential, and conversion elements characterize the activation and ohmic overpotentials comprised in η_{Ohm}. A coupling element subtracts the overpotentials to the E (Fig. 6).

The equations are dimensionally correct. Voltages are expressed in V, currents in A, the power in W, the current density in $A\ cm^{-2}$, the capacitance are stated in F, the inductors in H, the resistance is in Ω and the conductivity is in $S\ cm^{-1}$. The volumetric flow is expressed in $L\ min^{-1}$, the volume in m^3, the surface in cm^2, longitude are in cm, the temperature in K, and pressure in Pa.

3.2. Supercapacitor modeling

The model used to simulate the supercapacitor bank performance is a simplified arrangement of the EC proposed in [53], and the reduced model is shown in Fig. 7. The characteristic parameters were determined from the experimental measurements made in a *Maxwell* supercapacitor bank (Fig. 3). The output voltage is computed with Eq. (19).

$$V_{Sup} = I_{Sup} R_{ISR} + \frac{1}{C_{i0} + C_{i1} V_{Sup}} \int I_{Sup} dt \tag{19}$$

The EMR of the supercapacitor (Fig. 8) was built from the EC of Fig. 7: the capacitors and the internal resistance are represented using accumulation and conversion elements; moreover, a mono-physical coupling sums the capacitor voltage and the resistance voltage. The EC parameters are $R_{ISR} = 34\ m\Omega$, $C_{i0} = 305$ F and $C_{i1} = 10.5075$ F/V.

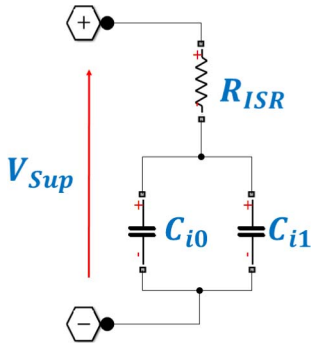

Fig. 7. Equivalent circuit model of the supercapacitor bank.

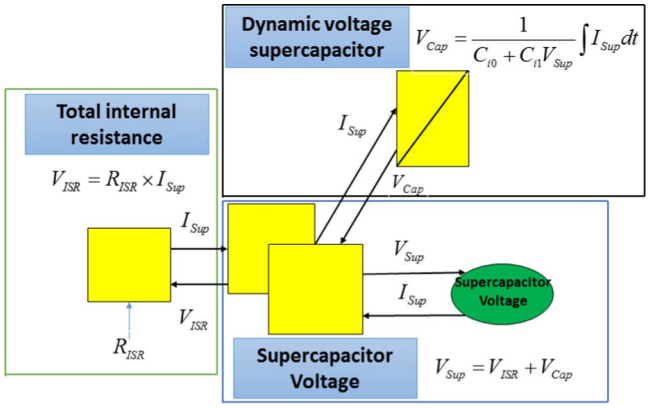

Fig. 8. EMR of the supercapacitor.

3.3. Power conditioning unit simulator

We considered a typical topology [39] to simulate the power conversion unit of the hybrid system (Fig. 9). Two inductors in series with the PEMFC and the supercapacitors connect the sources to their respective conversion unit, and the PEMFC is coupled to a boost

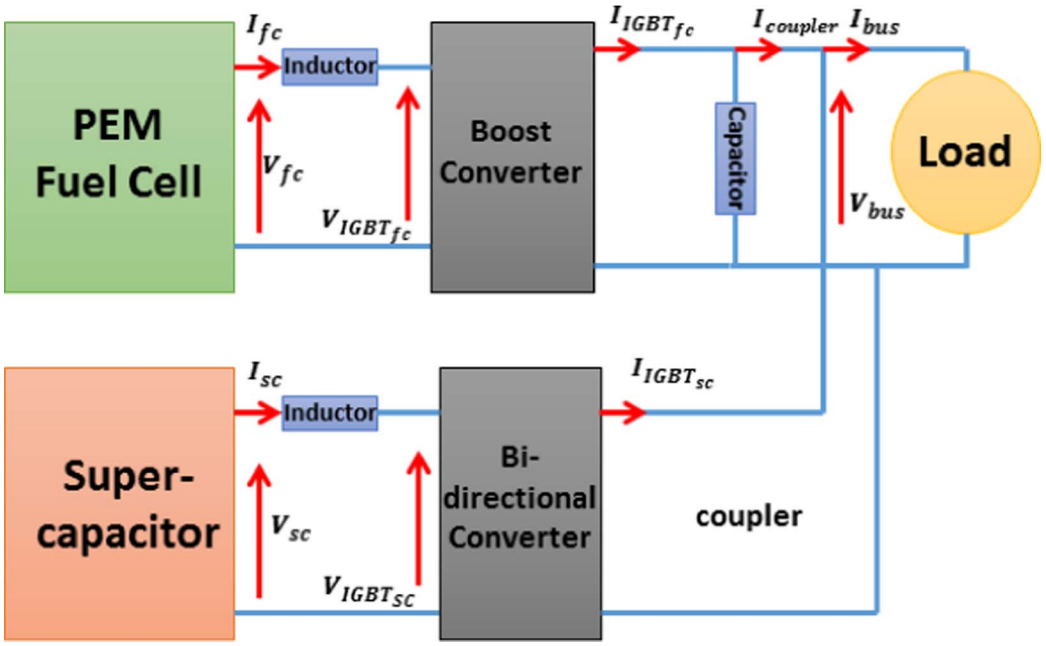

Fig. 9. Power conversion unit topology.

converter, while the supercapacitor needs a bidirectional converter for delivery and recovery cycles; we simulated these power-conditioning elements using ideal commutation devices (no losses or energy storage). A coupling capacitor connects the PEMFC, supercapacitor, and the load to a DC bus.

We built the EMR of the power conditioning unit using conversion elements to represent the converters; their corresponding equations are Eq. (20) for the PEMFC boost converter and Eq. (21) for the bidirectional converter of the supercapacitor. The parameter D is the duty cycle.

$$\begin{cases} V_{IGBT_{fc}} = D_{fc}\ V_{bus} \\ I_{IGBT_{fc}} = D_{fc}\ I_{bus} \end{cases} \tag{20}$$

$$\begin{cases} V_{IGBT_{sc}} = D_{sc}\, V_{bus} \\ I_{IGBT_{sc}} = D_{sc}\ I_{sc} \end{cases} \tag{21}$$

Energy-accumulation elements represent the inductors and the coupling capacitor. The equations relating the current and the voltage in the sources (I_{fc}–V_{fc},I_{sc}–V_{sc}) and the bus (I_{bus}–V_{bus}) are given in Eqs. (22)–(25). Coupling mono-physical elements interconnect in parallel the ensemble PEMFC-supercapacitor-power-conditioning unit (Fig. 10). For the sake of simplicity, the PEMFC and the supercapacitor are indicated as sources with green ovals in the EMR of Fig. 10.

$$I_{fc} = \frac{1}{L_{fc}} \int (V_{fc} - V_{IGBT_{fc}})dt \tag{22}$$

$$I_{sc} = \frac{1}{L_{sc}} \int (V_{sc} - V_{IGBT_{sc}})dt \tag{23}$$

$$V_{bus} = \frac{1}{C_{couple}} \int (I_{IGBT_{fc}} - I_{couple})dt \tag{24}$$

$$\begin{cases} I_{couple} = I_{bus} - I_{IGBT_{sc}} \\ V_{bus} = Common \end{cases} \tag{25}$$

4. Control of hybrid system

The control of the experimental PEMFC module includes the regulation of the stoichiometric oxygen excess ratio at a reference value of 1.5 and ideal control of temperature and relative humidity, i.e., maintaining constant values of 65 °C and 80%, respectively. For each source, there is a twofold loop control including an inner current control and the external voltage regulation.

We deduced the controllers using precise inversion rules. The EMR methodology simplifies the identification of the energy flows, and consequently, the design of inversion-based control. The EMR of the system contains blue parallelograms that symbolize the control elements.

4.1. Local control loops

The local control loops regulate the PEMFC and the supercapacitor currents. In both cases, the duty cycle is the manipulated variable. The inversion of the inductors and the power-conditioning unit blocks are defined in Eqs. (20) and (21) yield, (26) and (27) for the boost converter and bidirectional converter inversion, and Eqs. (28) and (29) for the inductors inversion. PI controllers C_1 and C_2 were tuned with the reaction curve method with the following calculated gains $K_p = -2.5395 \times 10^3$ and $K_i = 1.9496 \times 10^5$ for controller C_1 and $K_p = -2.8217 \times 10^3$ and $K_i = 1.7723 \times 10^5$ for controller C_2.

$$\begin{cases} D_{fc_{mo}} = \frac{V_{IGBT\,fc_{mo}}}{V_{bus}} \\ D_{sc_{mo}} = \frac{V_{IGBTsc_{mo}}}{V_{bus}} \end{cases} \tag{26}$$

$$\begin{cases} V_{IGBT\,fc_{mo}} = C_1[I_{fc_{ref}} - I_{fc_{med}}] + V_{fc_{med}} \\ V_{IGBTsc_{mo}} = C_2[I_{sc_{ref}} - I_{sc_{med}}] + V_{sc_{med}} \end{cases} \tag{27}$$

4.2. Power split control

We determined the power distribution between the sources using a first-order low-pass filter (see the scheme in Fig. 11), and the load is decomposed into two parts, the low-frequency load is required for the PEMFC and the high-frequency load is required for the SC. The core aim of this approach is deciding whether the electrical dynamic response of the sources is a low or high frequency. In fact, the cutoff frequency of the low-pass filter can be chosen over a span of frequencies. For a fuel cell-supercapacitor system, it is determined by the PEMFC performance owing to its slower response. Thus, the cutoff frequency should be associated with the fuel-cell dynamic characteristics, but it should also be

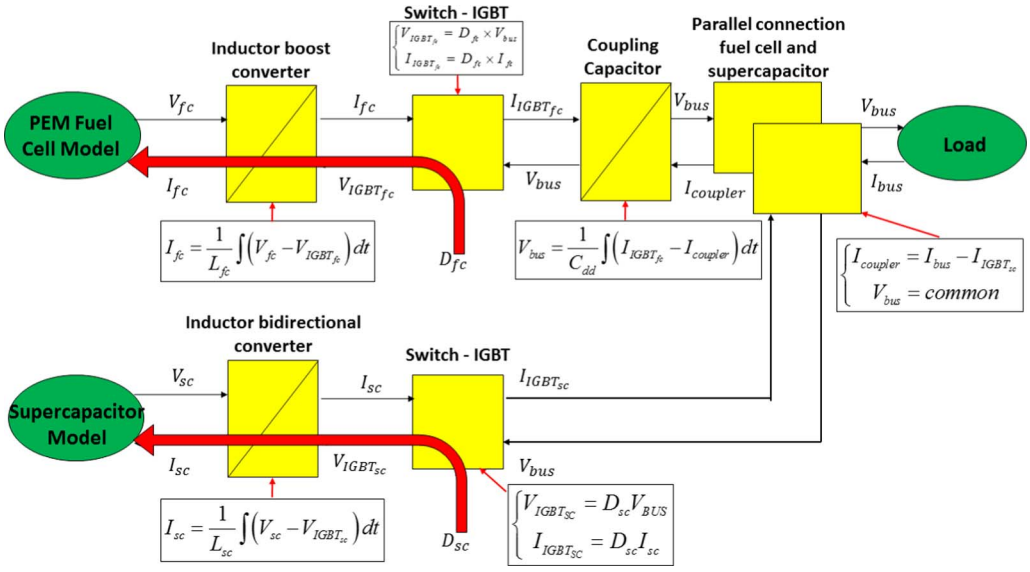

Fig. 10. EMR of the power conversion unit.

subject to the hybridization objectives. For real applications, we can determine the cut-off frequency by considering an analysis of PEMFC voltage-current measurements along with hybridization criteria defined by the designer.

A cautious estimation of the cutoff frequency was proposed in [54]. A Blackman-Tukey spectral analysis was performed for different oxygen stoichiometric excess ratio values, between 1.5 and 2.5, for input-output data measured on the *Bahia* PEMFC system. The Bode magnitude plot, which expresses the magnitude in *dB* of the frequency response, does not enable us to observe the high-frequency transfer function gains. Therefore, the PEMFC operation is limited to the region where it is more sensitive to load changes. The selected cutoff frequency of $0.05\,Hz$ defines an operating bandwidth that enables us to prevent abrupt changes in the fuel cell, and constrains its operation strictly in a safe region with respect to its electrical behavior.

To increase the PEMFC utilization, discrete Fourier analyses of the experimental voltage and current signals give information of higher frequency components (Fig. 12). For an oxygen stoichiometric excess ratio equal to 1.5, the representation in the frequency domain of the current demonstrates that the load solicits electrical energy to the PEMFC beyond 0.2 Hz; conversely, the representation in the frequency domain of the output voltage in Fig. 12 reveals that beyond 0.2 Hz, the response of the PEMFC decreases considerably; then, we chose this value as the cutoff frequency. The new value defines an operating bandwidth that enables us to benefit the PEMFC dynamic capacities as the main source by intensifying its utilization, while it continues to operate within safe limits.

Recapitulating, the effective cutoff frequency span for splitting the power between the *Bahia* PEMFC and the Maxwell SC bank is 0.05–0.2 Hz. In this study, the energy management is mainly evaluated for a cutoff frequency of 0.2 Hz, which increases the PEMFC operation as the main source, whereas the SC is mostly used to supply power surges. However, to evaluate the effect of varying the cutoff frequency on the energy-management performance, we made a comparison against power distributions based on cutoff frequencies of 0.05 and 0.1 Hz. The mitigation or elimination of the undesired transient phenomena in the PEMFC is expected to be achievable to different degrees, according to the selected cutoff frequency. Moreover, we proved the scenarios with two different loads that have different power distribution challenges.

We computed the current solicited to the sources using Eqs. (28) and (29) when the time constant of the low-pass filter is 0.7957 s. The control scheme is depicted in Fig. 13.

$$I_{fc} = \frac{P_{load}}{V_{fc}} \tag{28}$$

$$I_{sc} = \frac{P_{load}}{V_{sc}} \tag{29}$$

5. Results and discussion

We constructed the simulator using the EMR library developed at the University of Lille, France [55]. The programming platform contains blocks where the model equations are introduced with integral causality. The complete EMR of the hybrid power-supply system is presented in Fig. 14.

5.1. PEMFC model validation

In order to assess the validity of the PEMFC model, we measured input and output data in the *Bahia* PEMFC module under nominal operating conditions: temperature of 65 °C, stoichiometric oxygen excess ratio equal to 1.5, and relative humidity of 80%. We compared the

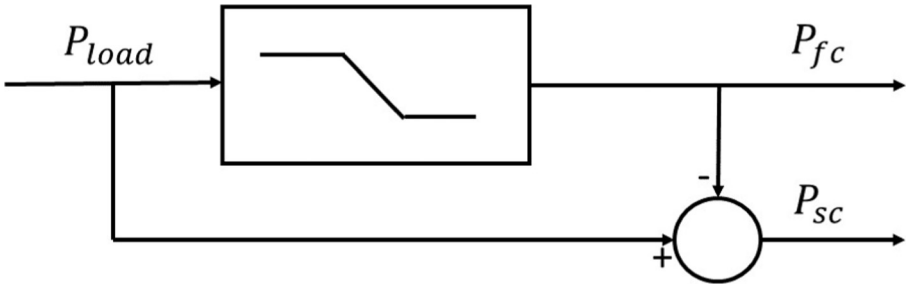

Fig. 11. Power split between the sources.

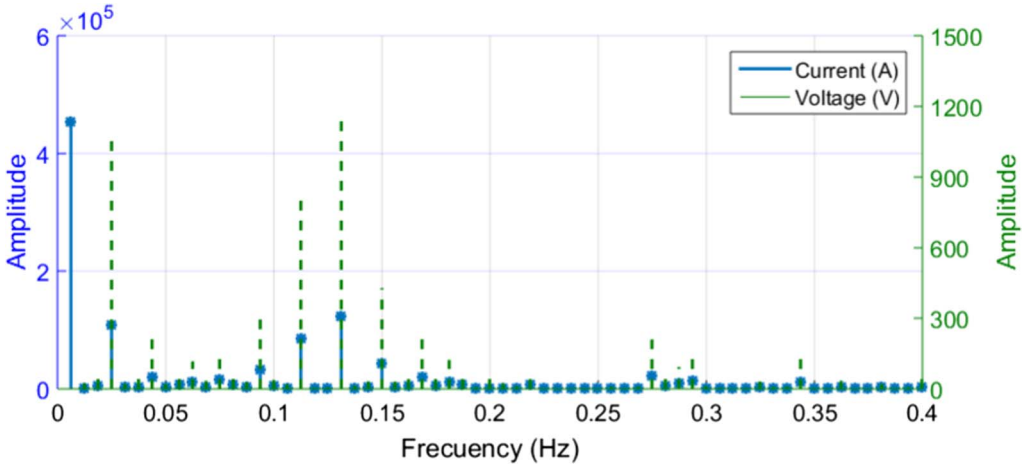

Fig. 12. Fourier analyses of experimental voltage (green) and current (blue) signals. (For interpretation of the references to color in this figure legend, the reader is referred to the web version of this article.)

model prediction using experimental measurements.

We evaluated the model efficacy with which to predict the performance of the PEMFC using a series of simulations, while applying three load profiles: a current pulse train (Fig. 15), a current ramp train (Fig. 16), and the New European Driving Cycle (NEDC) (Fig. 17), which was designed to represent typical European busy cities driving conditions. For the driving cycle test, the load-power profile is scaled to 1 kW in order to enable the evaluation of the hybrid system operation with load solicitations characteristic of vehicular applications.

We compared the calculated PEMFC output voltage with experimental data available from the *Bahia* module. The model responses were obtained for the three considered load profiles (Figs. 18–20). The resulting mean-squares errors (MSEs) of the PEMFC output voltage predictions are 0.1407, 0.1420, and 0.1463 for the pulse train, ramp train, and NEDC profiles, respectively. At steady state, the prediction error is negligible, as it can be seen in Fig. 21, where the polarization curve prediction and the experimental polarization curve are exhibited.

The model correctly predicts the transients due to the double-layer capacitance effect and the undershoot phenomenon. The results demonstrate that the model agrees well with the experimental transient and steady-state data.

5.2. Supercapacitor model validation

The initial state of the supercapacitor corresponds to a charge of 90% (14 V). We examined the supercapacitor model for recovery and delivery periods using the current profiles of Fig. 22a and b, respectively. The model response matches the experimental output voltage. The MSE is 0.1011 during the recovery test and 0.1285 during the delivery test (Fig. 23a and b).

5.3. Hybrid system simulation with power management and control

We evaluated the performance of the hybrid system and the adequacy of the energy-management strategy in the simulation environment for two load-power profiles: the first profile is the EPA Urban Dynamometer Driving Schedule (UDDS) (Fig. 24). The second profile is the pulse train of Fig. 15, which shows stiff load variations, which are susceptible to conducting the PEMFC to operate with undershoot problems; this is representative of turning-on and turning-off connected appliances. The simulation of the PEMFC includes the control of the stoichiometric oxygen excess ratio at a reference value of 1.5 and ideal control of temperature and relative humidity, i.e., maintaining constant values of 65 °C and 80%, respectively.

To show the advantages of the hybridization, we present the simulation results and compare them for two cases: the entire load profiles (before being split) are applied to simulate the PEMFC-boost converter system as a single-source system; afterwards, we applied the split load profiles to simulate the complete hybrid powertrain with the energy-management strategy implemented. In this case, the current

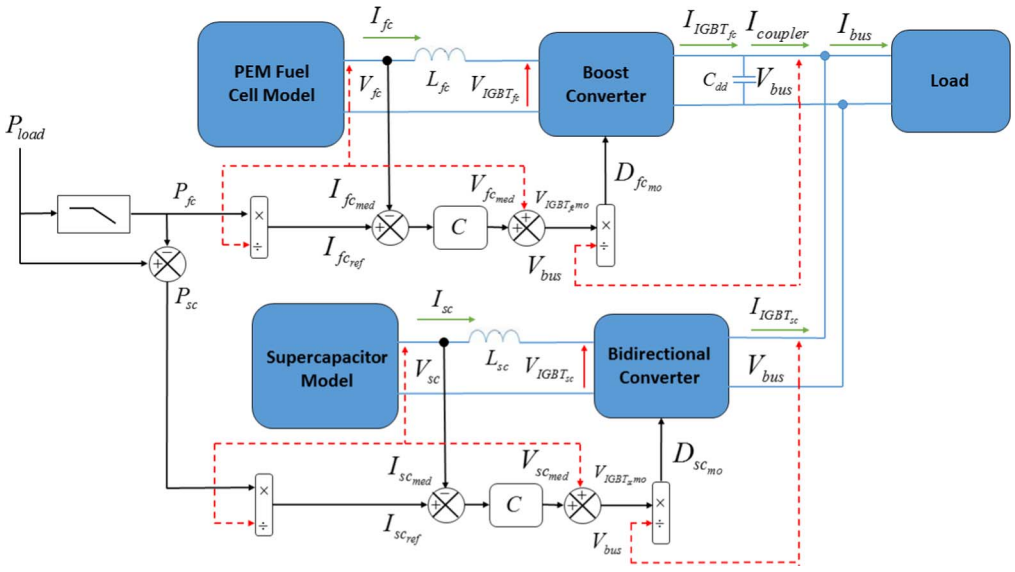

Fig. 13. Block diagram of the control scheme for the hybrid-generation system.

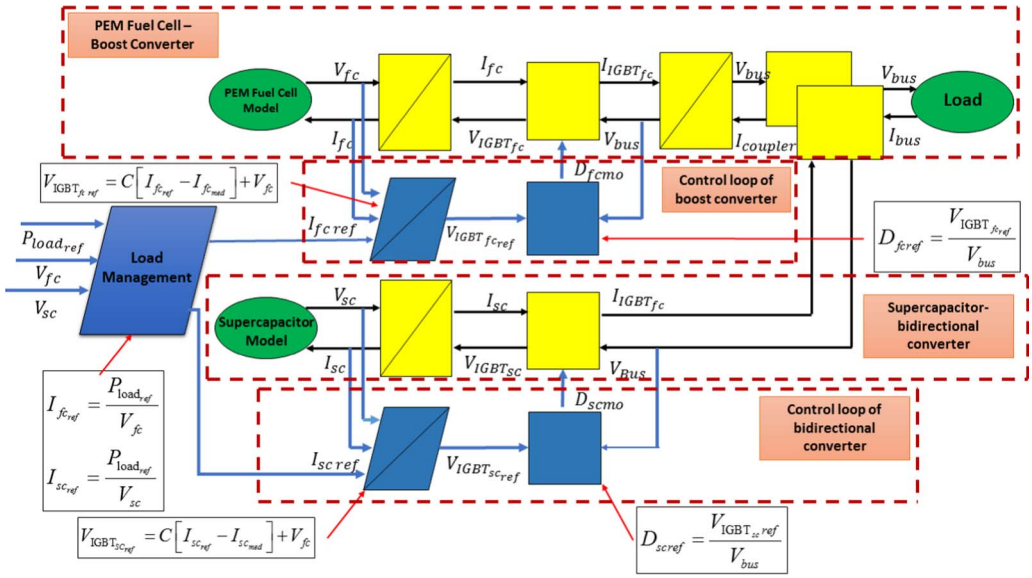

Fig. 14. EMR of the hybrid powertrain.

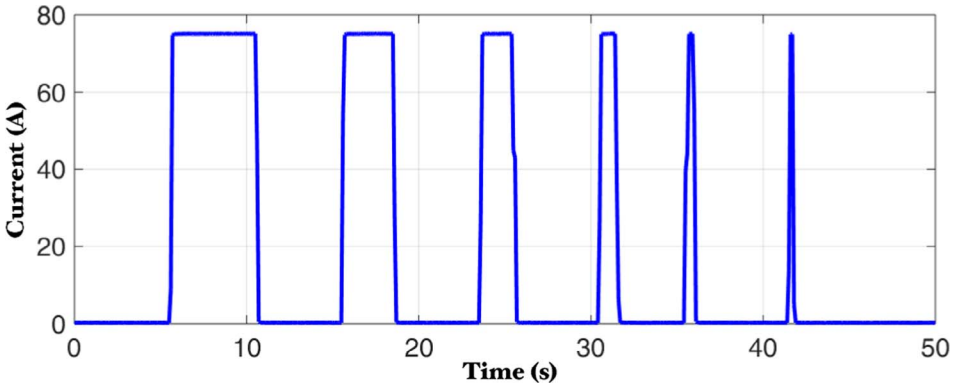

Fig. 15. Pulse train current required for the PEMFC.

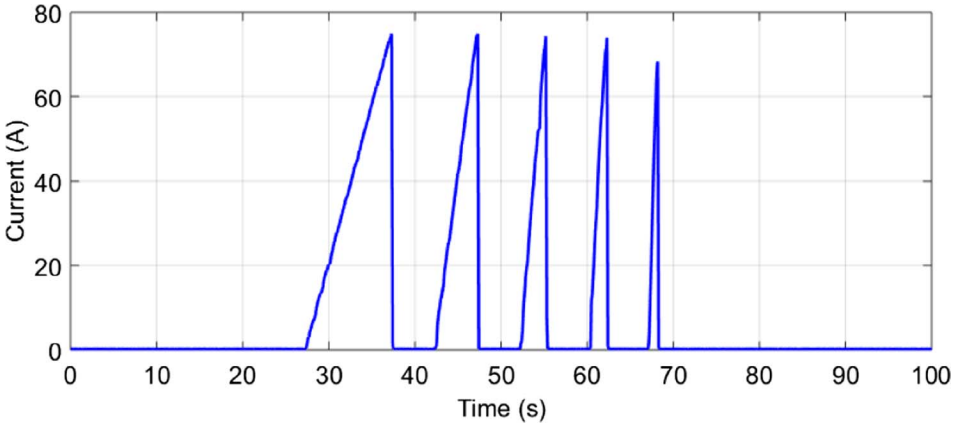

Fig. 16. Ramp train current demanded to the PEMFC.

required by the PEMFC is determined according to the split criterion to separate the low- and high-frequency current demands.

We conducted a first series of simulations under UDDS cycle solicitations (Fig. 24). Primarily, Fig. 25a exhibits the single PEMFC operation (green lines), which is compared with the hybrid powertrain operation for power splits that are determined by cutoff frequencies of 0.05 and 0.2 Hz (blue and orange lines, respectively). A zoom between 150 and 250 s (Fig. 25b) simplifies the comparison between two power-distribution proposals. The results prove that the power-split strategy of the hybrid powertrain guarantees smoother loads for the PEMFC than those required for the PEMFC as a single source, especially if we use smaller cutoff frequencies. Likewise, the simulations support the fact that the cutoff frequency of 0.2 Hz allows a maximal utilization of the fuel cell at the same time that its performance evolves in the whole current safe range, and this is because it operates until 65 A and supplies 80% of the required power. We calculated this participation as the proportion of the average global power required by the load that is delivered by the fuel cell during the simulation time (blue lines in Fig. 26). After the filter, the SC has a greater contribution during speedup, allowing the fuel cell to respond with its slower dynamic capacity, whereas for the periods without sudden bursts of speed, the PEMFC supplies almost all of the required power (Fig. 26). On the other

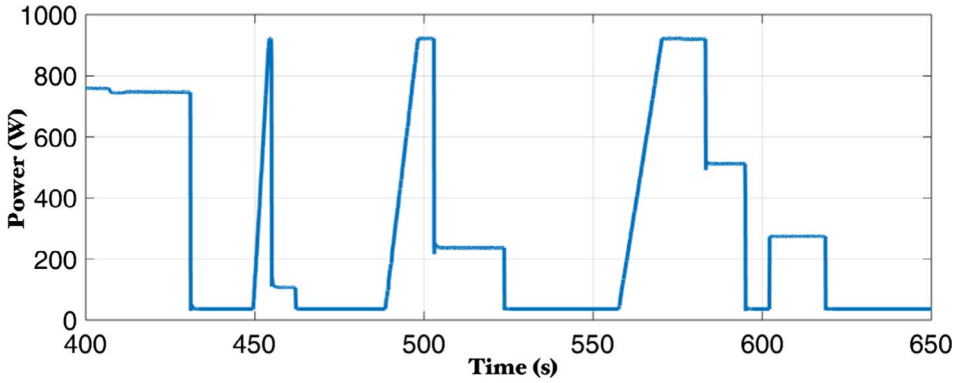

Fig. 17. NEDC for busy European cities.

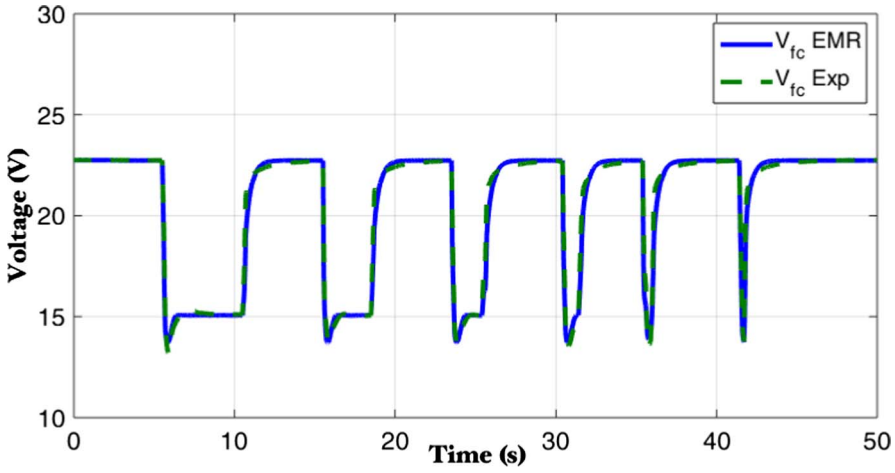

Fig. 18. PEMFC response under a step-train current demand.

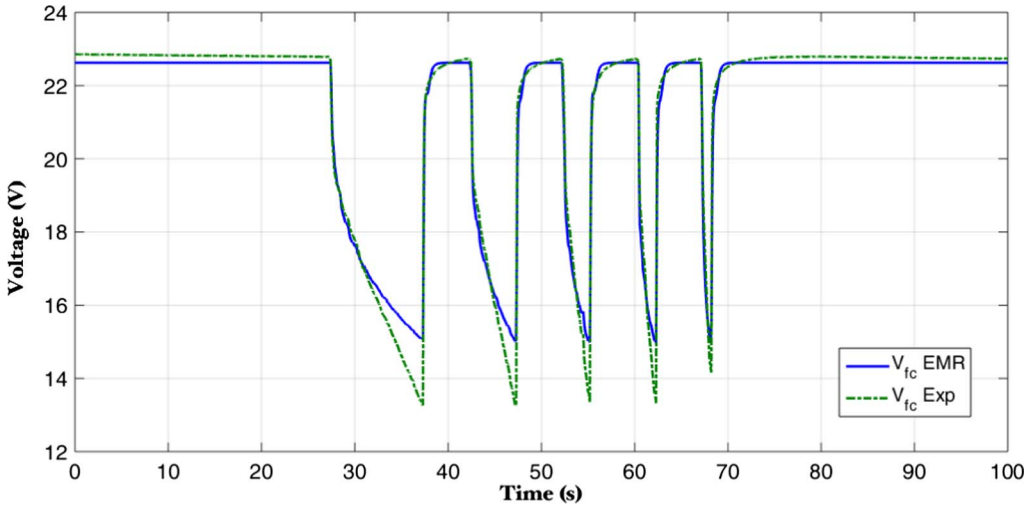

Fig. 19. PEM fuel cell response under a ramp-train current demand.

hand, the cutoff frequency of 0.05 Hz offers better conditions with respect to the number of startups and shutdowns, and this number decreases as the cutoff frequency decreases; for example, the PEMFC operation without power-management control has around eight startups and shutdowns in the period between 0 and 130 s (Fig. 25a). A power distribution determined with a cut-off frequency of 0.2 Hz reduces this number to around five, but a cut-off frequency of 0.05 Hz leads to delivery currents that are higher than zero during the entire period under consideration (Fig. 25a).

We conducted a second series of simulations using pulse-train solicitations (Fig. 15). We estimated the SOC variation and the PEMFC electrical efficiency online for three chosen cutoff frequencies during the simulation of the hybrid generator operation. First, Fig. 27 shows the single PEMFC response (green lines), compared with the hybrid powertrain performance for cutoff frequencies of 0.05 Hz (yellow), 0.1 Hz (orange), and 0.2 Hz (blue).

The PEMFC operating as a single source clearly undergoes voltage undershoot. An additional reduction of 4 V represents a further voltage drop of 22%. Conversely, irrespective of the cutoff frequency value, the hybrid generator leads to the elimination of the voltage undershoot phenomenon during step-up transients. In the same way as the previous case (UDDS cycle tests), the energy distribution between the sources moderates the input at the fuel-cell terminals, but for the pulse-train test, it is also evident that the strategy benefits the oxygen-starvation

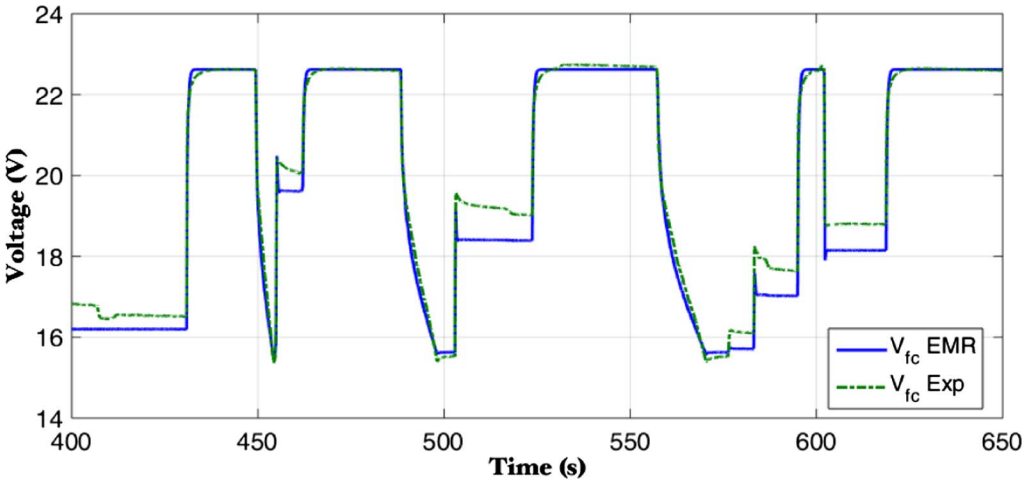

Fig. 20. PEM fuel cell response to the NEDC power profile.

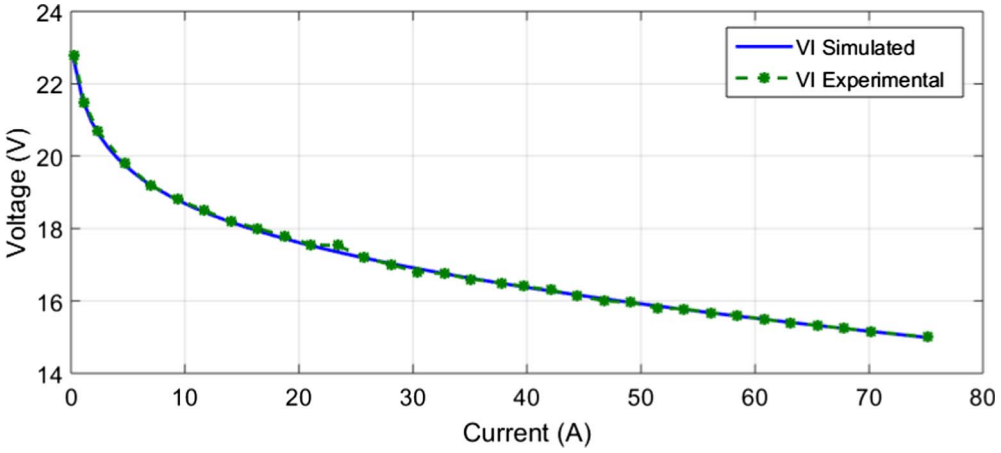

Fig. 21. Experimental and estimated polarization curve (steady state performance) of the PEMFC.

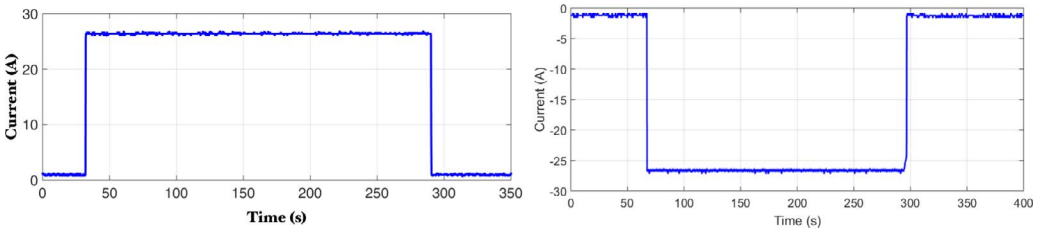

(a) Recovery cycle. (b) Delivery cycle.

Fig. 22. Supercapacitor current demand and delivery.

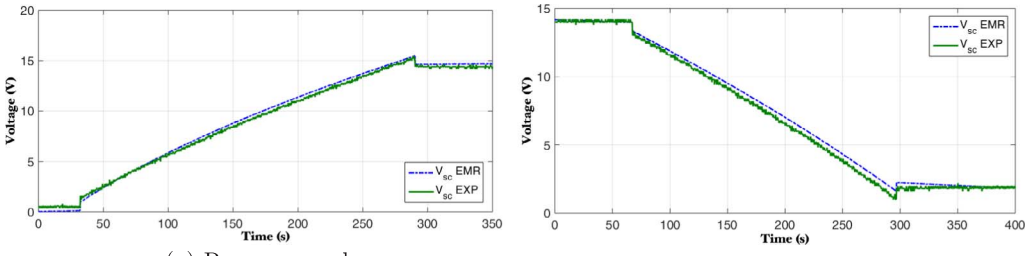

(a) Recovery cycle. (b) Delivery cycle.

Fig. 23. Supercapacitor response under current demand and delivery.

mitigation and reduces the risk of physical damage in the polymeric membrane, while still promoting the PEMFC operation within the safe region of the polarization curve. However, the current demand evolution is smoother as the cutoff frequency decreases, and so the voltage evolution. On the other hand, as the cutoff frequency decreases, the operating range is also reduced; for example, the power split obtained using a cutoff frequency of 0.05 Hz decreases the maximum required current to approximately 60 A (*vs.* 75 A obtained with a cutoff frequency of 0.2 Hz).

For the same load conditions, Fig. 28 shows the current required by the supercapacitor and its associated voltage. Positive values correspond to delivery periods, while negative values correspond to recovery

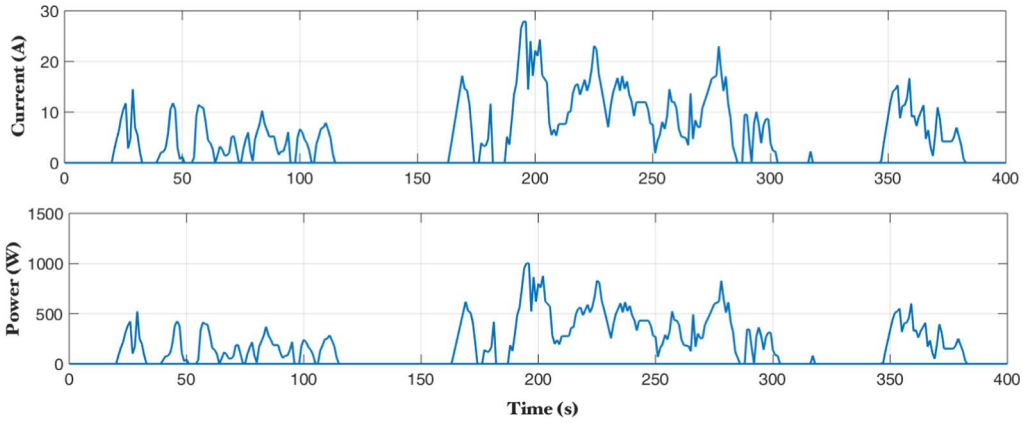

Fig. 24. UDDS cycle.

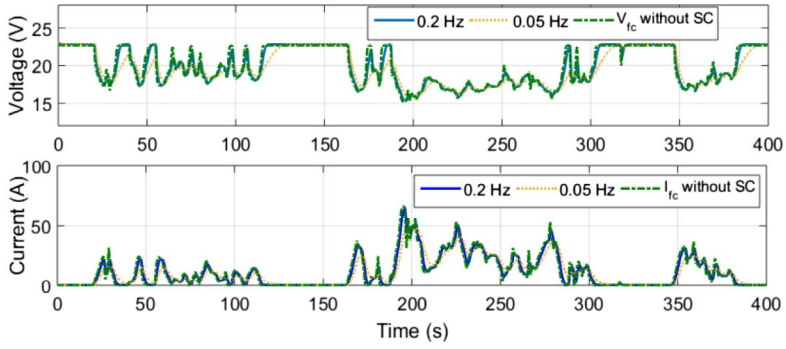

(a) Single PEMFC operation *vs.* hybrid system operation.

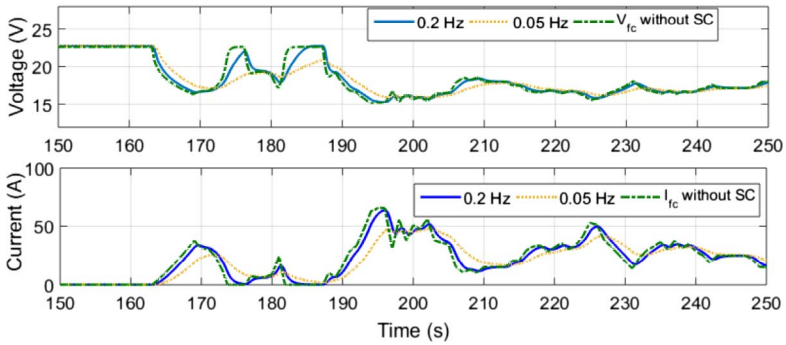

(b) Comparison of the power split between 150 and 250 s for two cut-off frequencies.

Fig. 25. Simulation of the energy management for UDDS cycle.

periods. It can also be seen that startups and shutdowns do not occur abruptly, given that the fuel cell is delivering energy to the SC instead of turning-off when no load is required. Then, we achieve a smoother but continuous operation.

With regard to the backup source, it is not easy to estimate the SOC because rapid charging or discharging of these devices produces non homogeneous regions and charge re-distribution side-effects in the electrodes [56]. Therefore, it is feasible to consider the control of the supercapacitor terminal voltage for indirect regulation of the SOC, and reduce SC damage risk. Moreover, supercapacitors operate over a wider voltage range than batteries do, and can work at voltage values below its maximum operating value. The utilized supercapacitor model is simple and does not evaluate the SOC, but a rough approximation is provided by (30).

$$SOC = 100\left(\frac{Q_0 - \int_0^t i(\tau)d\tau}{Q_T}\right) \tag{30}$$

SOC = State of charge (%).
Q_0 = Initial charge (C).
Q_T = Total charge (C).
$i(\tau)$ = Current (A).

The target is to keep the SC voltage around 14 V, which corresponds to 90% of the maximal charge. More precisely, the voltage varies from 12 to 15.5 V (Fig. 28), or equivalently between 75% and 96.8% of the maximum SC terminal voltage value. The designed local control establishes the SC voltage around 14 V. Under these circumstances, the SOC varies between 86.7% and 87.7% if the power split is achieved with a cutoff frequency of 0.2 Hz, but it can be reduced to 85% with a

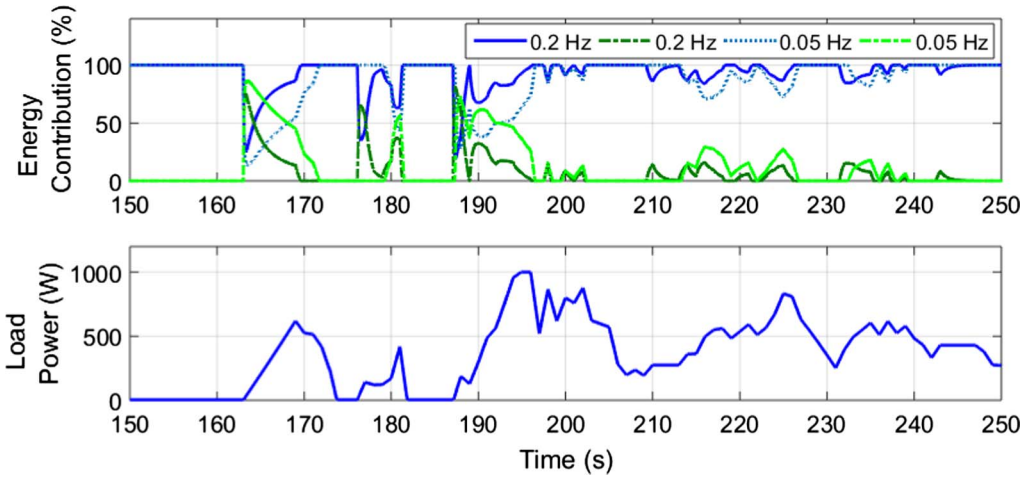

Fig. 26. Power split between the PEMFC (blue) and the SC (green) for two cut-off frequencies during a UDDS cycle. (For interpretation of the references to color in this figure legend, the reader is referred to the web version of this article.)

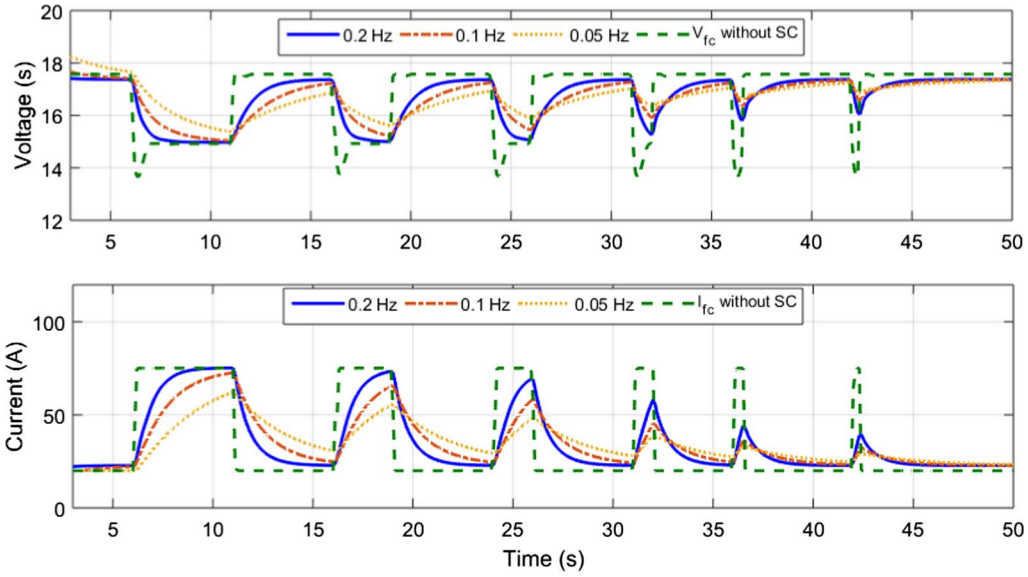

Fig. 27. Single PEMFC operation *vs.* hybrid system operation for a pulse-train load. Comparison of power split for three cut-off frequencies.

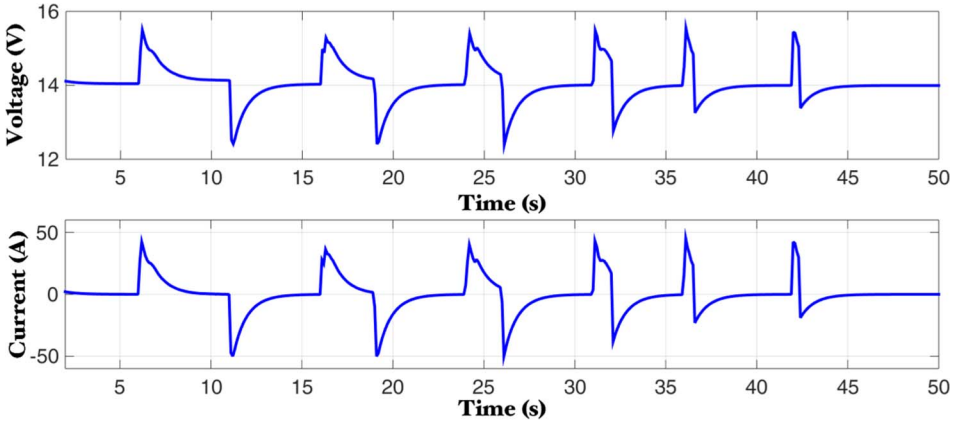

Fig. 28. Supercapacitor recovery-delivery after power split for a pulse-train load.

cutoff frequency of 0.05 Hz (Fig. 29), whereas the SOC calculated for the previous UDDS cycle test varies from 86.8% to 87.9% for a cutoff frequency of 0.2 Hz; for simplicity, this plot is not presented here.

With respect to the PEMFC efficiency, Fig. 30 shows the LHV electrical efficiency of the PEMFC. During step-up transients, the efficiency of the hybrid powertrain increases compared with the efficiency of PEMFC as a single source, particularly as the cutoff frequency becomes smaller. For step-down transients, the fuel-cell operation is reduced over the activation region (highest voltage zone), contrary to the dynamic behavior observed if the SC is not used as a backup source. The last issue should be useful to define a lower operating limit for the PEMFC, as explained in the following paragraph.

The previous remarks concerning the electrical efficiency estimation are valid for the tests with the UDSS cycle. The oxygen consumption is reduced, especially under abrupt load changes, and the voltage overshoot is eliminated while the PEMFC electrical LHV efficiency remains

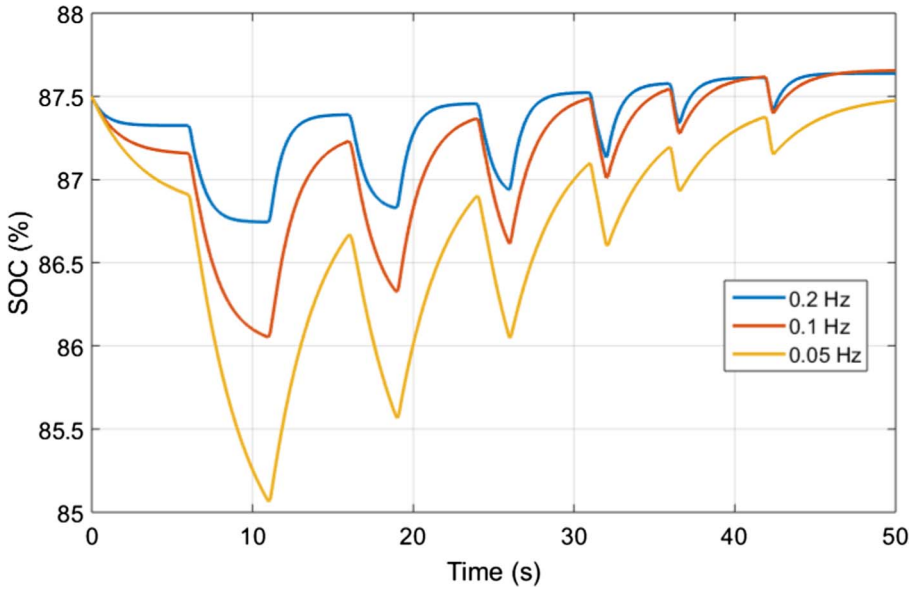

Fig. 29. The SC SOC for three cut-off frequencies.

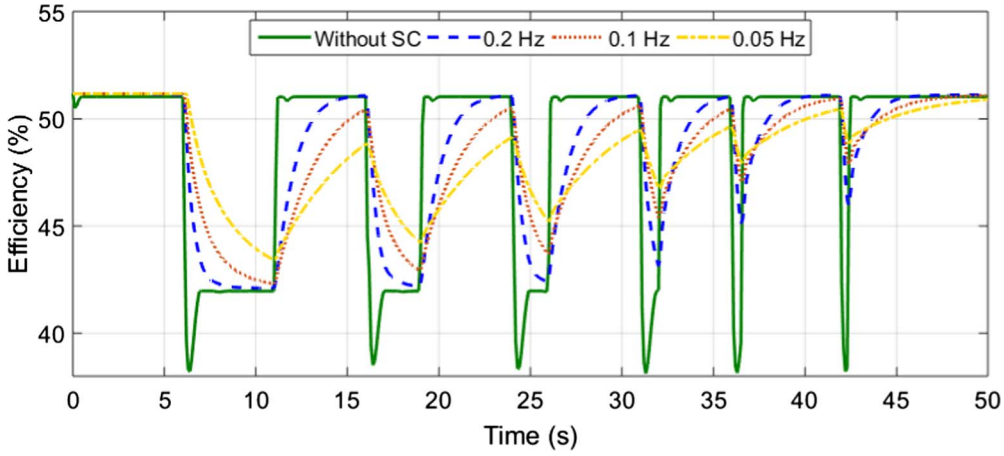

Fig. 30. PEMFC efficiency for three cut-off frequencies.

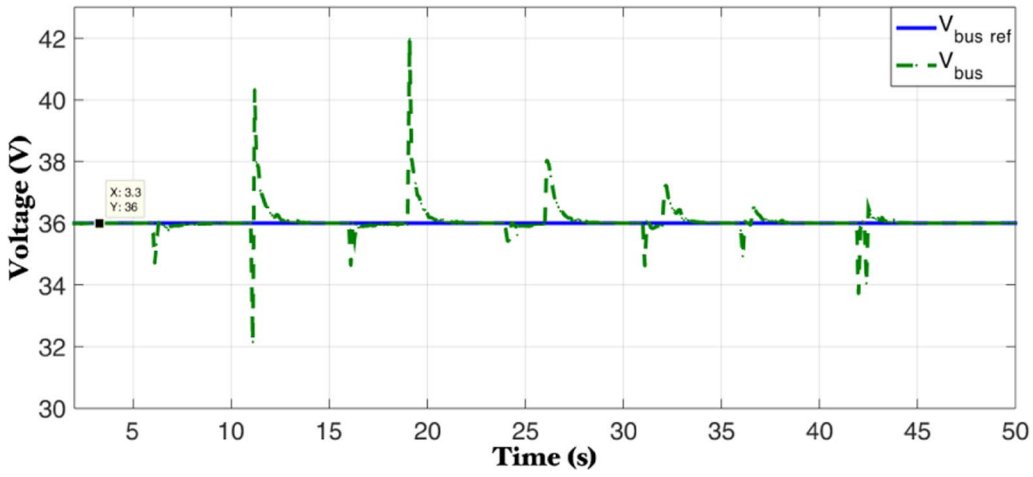

Fig. 31. Bus voltage control (step pulsed train) for a cut-off frequency of 0.2 Hz.

between 40% and 65%. The activation and concentration zones are thus avoided. In fact, the split control imposes on the hybrid powertrain an upper bound that constrains adequately the PEMFC electrical behavior. With respect to the definition of a reliable lower bound, the performance of the compressor delivering the air (oxygen) to the fuel cell and its control should be considered because currents close to zero or small currents would lead to mechanical instabilities ([57]); meanwhile, to address this task, the additional modeling of auxiliary elements should also be integrated into the built hybrid generator simulator.

As shown in Figs. 24–28, the voltage of the sources moves away from the bus voltage; hence, the converters elevate the voltage and the global control regulates appropriately the bus voltage at the reference

value of 36 V Fig. 31.

For both load-profile tests, the boost elevator and the bidirectional converter guarantees the recovery and delivery periods, enabling them to operate the supercapacitor at voltage values around 90% of the maximum value, and then to regulate the bus voltage. In addition, the regulation of the stoichiometric oxygen excess ratio at a reference value was consistently achieved.

6. Conclusions

The dynamic simulator of the hybrid power-supply system combines experimentally validated PEMFC and SC EC models. The PEMFC EC model matches the double-layer capacitance and the voltage-undershoot transients, which are typically encountered in electrochemical devices. The novelty of the PEMFC dynamic model is that the prediction of the transient behavior depends explicitly on the operating conditions because temperature and gas-flow dependent parameters were introduced, whereas typical EC models contain constant parameters or rare current-dependent parameters that capture indirectly the effect of the operating conditions. Another difference is that the undershoot prediction is integrated within the EC model by introducing a set capacitor-inductor with a second-order response. The EMR methodology enables the integration of inherent control elements facilitating the deduction of inversed-based control loops, and the developed EMR-based simulator guaranties the trade-off between simplicity and phenomenological considerations to study the multiphysical system.

Nowadays, a number of studies related to PEMFC technology focus on both practical and theoretical aspects of hybrid-system development and design. The originality of this study lies in the thorough assessment aimed at measuring the influence of the power split between the PEMFC and the SC on the hybrid-generator performance, because we discussed different practical implications for real applications based on the following proposals: (1) An effective cutoff frequency range was defined using data from a PEMFC experimental module that was treated with two different frequency representations. (2) For a reduced scale of 1 kW, the simulation tests include typical conditions of electric vehicles, as well as turning-on/turning-off connected appliances that offer different hybridization challenges. (3) A quantitative study of the effect of the cutoff frequency was possible because the prediction of real static and dynamic characteristic behaviors of the sources was achieved, including the estimation of the SC SOC and the PEMFC electrical LHV efficiency. (4) Furthermore, the performance evaluation and comparison of the proposed power split configurations were achieved in terms of the prevention of undesired transients, causing failure and degradation in real systems.

As a result, the proposed hybridization criteria are shown to improve the powertrain performance for a maximal profit of the PEMFC dynamic and power capacities by defining a high cutoff frequency (0.2 Hz), or for a reduced utilization that enhances the PEMFC transient behavior by defining a smaller cutoff frequency (0.05 Hz), because startups and shutdowns are reduced along with the fuel consumption. For the three cutoff frequencies considered, the PEMFC response is smooth, and is close to the Ohmic region. The undershoot and subsequent oxygen-starvation problems are eliminated in the PEMFC with respect to the operation whether the SC is incorporated as a backup source. To design the energy-management strategy, we considered simple power-conditioning systems and local control loops, including the stoichiometric oxygen excess ratio regulation, and the bus-voltage control that guarantees the bus reference value of 36 V, imposing short settling times and small overshoots.

Acknowledgment

The authors would like to thank SEP-CONACYT for support this project under Grant CB-2013/221988 and project 252003 “Programa de Redes Temáticas (RTH2).” The authors are also grateful to the École National d’Arts et Métiers for its valuable support with respect to experimental tests and for the facilities to use their laboratory equipment and resources. *José Francisco Gómez Aguilar* and *Victor M. Alvarado* acknowledge the support provided by CONACYT: cátedras CONACYT para jóvenes investigadores 2014.

References

[1] Wu H-W. A review of recent development: transport and performance modeling of PEM fuel cells. Appl Energy 2016;165:81–106.
[2] Olatomiwa L, Mekhilef S, Ismail M, Moghavvemi M. Energy management strategies in hybrid renewable energy systems: a review. Renew Sustain Energy Rev 2016;62:821–35.
[3] Bocklisch T. Hybrid energy storage systems for renewable energy applications. Energy Proc 2015;73:103–11.
[4] Boscaino V, Miceli R, Capponi G, Galluzzo GR. A review of fuel cell based hybrid power supply architectures and algorithms for household appliances. Int J Hydrogen Energy 2014;39:1195–209.
[5] Tie SF, Tan CW. A review of energy sources and energy management system in electric vehicles. Renew Sustain Energy Rev 2013;20:82–102.
[6] Ettihir K, Boulon L, Agbossou K. Optimization-based energy management strategy for a fuel cell/battery hybrid power system. Appl Energy 2016;163:142–53.
[7] Dash V, Bajpai P. Power management control strategy for a stand-alone solar photovoltaic-fuel cell-battery hybrid system. Sustain Energy Technol Assess 2015;9:68–80.
[8] Santucci A, Sorniotti A, Lekakou C. Power split strategies for hybrid energy storage systems for vehicular applications. J Power Sour 2014;258:395–407.
[9] Hwang J-J, Chen Y-J, Kuo J-K. The study on the power management system in a fuel cell hybrid vehicle. Int J Hydrogen Energy 2012;37:4476–89.
[10] Feroldi D, Serra M, Riera J. Energy management strategies based on efficiency map for fuel cell hybrid vehicles. J Power Sour 2009;190:387–401.
[11] Nasri S, Sami BS, Cherif A. Power management strategy for hybrid autonomous power system using hydrogen storage. Int J Hydrogen Energy 2016;41:857–65.
[12] Hemi H, Ghouili J, Cheriti A. Combination of markov chain and optimal control solved by pontryagins minimum principle for a fuel cell/supercapacitor vehicle. Energy Convers Manage 2015;91:387–93.
[13] Hemi H, Ghouili J, Cheriti A. A real time fuzzy logic power management strategy for a fuel cell vehicle. Energy Convers Manage 2014;80:63–70.
[14] Karami N, Moubayed N, Outbib R. Energy management for a PEMFC-PV hybrid system. Energy Convers Manage 2014;82:154–68.
[15] Lee SC, Kwon O, Thomas S, Park S, Choi G-H. Graphical and mathematical analysis of fuel cell/battery passive hybridization with k factors. Appl Energy 2014;114:135–45.
[16] Garca P, Torreglosa JP, Fernndez LM, Jurado F. Control strategies for high-power electric vehicles powered by hydrogen fuel cell, battery and supercapacitor. Expert Syst Appl 2013;40:4791–804.
[17] Barelli L, Bidini G, Ottaviano A. Optimization of a PEMFC/battery pack power system for a bus application. Appl Energy 2012;97:777–84 [Energy Solutions for a Sustainable World - Proceedings of the Third International Conference on Appl Energy, May 16–18, 2011 - Perugia, Italy].
[18] Pei P, Chen H. Main factors affecting the lifetime of proton exchange membrane fuel cells in vehicle applications: a review. Appl Energy 2014;125:60–75.
[19] Wang F, Yang D, Li B, Zhang H, Hao C, Chang F, et al. Investigation of the recoverable degradation of PEM fuel cell operated under drive cycle and different humidities. Int J Hydrogen Energy 2014;39:14441–7.
[20] Tang Y, Yuan W, Pan M, Li Z, Chen G, Li Y. Experimental investigation of dynamic performance and transient responses of a kw-class PEM fuel cell stack under various load changes. Appl Energy 2010;87:1410–7.
[21] Dou M, Hou M, Liang D, Shen Q, Zhang H, Lu W, et al. Behaviors of proton exchange membrane fuel cells under oxidant starvation. J Power Sour 2011;196:2759–62.
[22] Travassos MA, Rangel C. Polarity reversal in PEM fuel cells by fuel starvation. In: 3° Seminário Internacional de Torres Vedras 2010, hydrogen energy and sustainability-advances in fuel cell and hydrogen workshop. Portugal. p. 48–52.
[23] Verma A, Pitchumani R. Influence of membrane properties on the transient behavior of polymer electrolyte fuel cells. J Power Sour 2014;268:733–43.
[24] Hautier J-P, Faucher J, Caron J-P. Le Graphe Informationnel Causal, un outil pour analyser, comprendre, représenter. Journées 3EI, Cachan 1999:308.
[25] Bouscayrol A. Formalisme de Représentation et de Commande Appliqués aux Systèmes Electromécaniques Multimachines Multiconvertissuers, HDR thesis; Université des Sciences et Technologies de Lille; 2003.
[26] Bouscayrol A, Barrade P, Boulon L, Chen K, Cheng Y, Delarue P, et al. Teaching drive control using Energetic Macroscopic Representation Summer schools. In: Proceedings of the 14th European Conference on power electronics and applications. IEEE, Birmingham; 2011. p. 6.
[27] Barrade P, Bouscayrol A. Energetic macroscopic representation - an energy-flow based methodology dedicated for the control of multiphysics systems, Technical Report. CEDRAT, Lussane; 2011.
[28] Barrade P, Bouscayrol A. E.M.R. - an energy-flow based methodology dedicated for the control of multiphysics systems, Technical Report 62. October, CEDRAT; 2011.
[29] Bouscayrol A, Delarue P, Giraud F, Guillaud X, Kestelyn X, Lemaire-Semail B, et al. Teaching drive control using Energetic Macroscopic Representation - expert level. In: 13th European conference on power electronics and applications. Barcelona:

IEEE; 2009. p. 1–9.
[30] Depature C, Boulon L, Sicard P, Fournier M. Simulation model of a multi-stack fuel cell system. In: 15th European conference on power electronics and applications (EPE). Lille; 2013. p. 1–10.
[31] Boulon L, Agbossou K, Hissel D, Sicard P, Bouscayrol A, Péra M-C. A macroscopic PEM fuel cell model including water phenomena for vehicle simulation. Renew Energy 2012;46:81–91.
[32] Boulon L, Hissel D, Bouscayrol A, Péra M-C. From modeling to control of a PEM fuel cell using energetic macroscopic representation. IEEE Trans Indust Electron 2010;57:1882–91.
[33] Chrenko D. Energetic macroscopic representation modeling and control of a low temperature fuel cell system fed by hydrocarbons, Theses. Université de Franche-Comté; 2008.
[34] Chrenko D, Péra M, Hissel D. Fuel cell system modeling and control with energetic macroscopic representation. In: International symposium on industrial electronics, ISIE. Vigo: IEEE; 2007. p. 169–74.
[35] Agbli K, Péra M, Hissel D, Rallières O, Turpin C, Doumbia I. Multiphysics simulation of a PEM electrolyser: energetic macroscopic representation approach. Int J Hydrogen Energy 2011;36:1382–98.
[36] Jia F, Guo L, Liu H. Dynamic characteristics and mitigations of hydrogen starvations in proton exchange membrane fuel cells during start-ups. Int J Hydrogen Energy 2014;39:12835–41.
[37] Kim DK, Koh JS, Kim MS, Song HH. Experimental and computational study on the dynamic interaction between load variation and back pressure control in a polymer electrolyte membrane fuel cell for automotive application. Int J Hydrogen Energy 2015;40:12370–81.
[38] Wang Y-X, Xuan D-J, Kim Y-B. Design and experimental implementation of time delay control for air supply in a polymer electrolyte membrane fuel cell system. Int J Hydrogen Energy 2013;38:13381–92.
[39] Boulon L, Pera M, Hissel D, Bouscayrol A, Delarue P. Energetic macroscopic representation of a fuel cell-supercapacitor system. In: Vehicle power and propulsion conference, VPPC. Arlington (TX): IEEE; 2007. p. 290–7.
[40] Boulon L, Hissel D, Bouscayrol A, Pera M, Delarue P. Multi physics modelling and representation of power and energy sources for hybrid electric vehicles. In: Vehicle power and propulsion conference, VPPC. Harbin: IEEE; 2008. p. 1–6.
[41] Azib T, Remy G, Bethoux O, Marchand C. Control strategy with saturation management of a fuel cell/ultracapacitors hybrid vehicle. ni: Vehicle power and propulsion conference (VPPC). Lille: IEEE; 2010. p. 1–6.
[42] Castaings A, Lhomme W, Trigui R, Bouscayrol A. Comparison of energy management strategies of a battery/supercapacitors system for electric vehicle under real-time constraints. Appl Energy 2016;163:190–200.
[43] Gauchia L, Bouscayrol A, Sanz J, Trigui R, Barrade P. Fuel cell, battery and supercapacitor hybrid system for electric vehicle: modeling and control via energetic macroscopic representation. In: Vehicle power and propulsion conference (VPPC). Chicago (IL): IEEE; 2011. p. 1–6.
[44] Badji A, Djoudi H, Benyahia N, Denoun H, Zaouia M, Benamrouche N. Energetic macroscopic representation (EMR) based on internal model control (IMC) for fuel cell and supercapacitor hybrid electric vehicles. In: 3rd International conference on control, engineering & information technology (CEIT). Tlemcen: IEEE; 2015. p. 1–6.
[45] Chen K, Bouscaryrol A, Lhomme W. Energetic macroscopic representation and inversion-based control: application to an electric vehicle with an electrical differential. J Asian Electr Veh 2008;6:1097–102.
[46] Boulon L, Hissel D, Péra MC., Pape O, Bouscayrol A. Energy based modeling of a 6-wheel drive hybrid heavy truck. In: 5th IEEE vehicle power and propulsion conference, VPPC '09. p. 1316–21.
[47] Silva LI, Bouscayrol A, De Angelo CH, Lemaire-Semail B. Coupling bond graph and energetic macroscopic representation for electric vehicle simulation. Mechatronics 2014;24:906–13.
[48] Xing L, Cai Q, Xu C, Liu C, Scott K, Yan Y. Numerical study of the effect of relative humidity and stoichiometric flow ratio on PEM (proton exchange membrane) fuel cell performance with various channel lengths: an anode partial flooding modelling. Energy 2016;106:631–45.
[49] Meidanshahi V, Karimi G. Dynamic modeling, optimization and control of power density in a PEM fuel cell. Appl Energy 2012;93:98–105.
[50] Hou Y, Yang Z, Wan G. An improved dynamic voltage model of PEM fuel cell stack. Int J Hydrogen Energy 2010;35:11154–60 [Hyceltec 2009 Conference].
[51] Escobedo Hernández E, Zamora Campos LA. Modelado dinámico de celdas de combustible, Master's thesis. TecNM/CENIDET, Mexico; 2006.
[52] Pukrushpan J, Stefanopoulou A, Peng H. Modeling and control for PEM fuel cell stack system. In: Proceedings of the American control conference, vol. 4; 2002. p. 3117–22.
[53] Zubieta L, Bonert R. Characterization of double-layer capacitors for power electronics applications. IEEE Trans Indust Appl 2000;36:199–205.
[54] Sandoval C, Alvarado VM, Carmona J-C, Lopez GL, Gomez-Aguilar J. Energy management control strategy to improve the fc/sc dynamic behavior on hybrid electric vehicles: a frequency based distribution. Renew Energy 2017;105:407–18.
[55] EMR website; 2016 < http://emr.univ-lille1.fr/ > [Online; accessed 22-February-2016].
[56] Nadeau A, Sharma G, Soyata T. State-of-charge estimation for supercapacitors: a kalman filtering formulation. In: International conference on acoustics, speech and signal processing (ICASSP). IEEE; 2014. p. 2194–8.
[57] Cruz Rojas A, Lopez G Lopez, Gomez-Aguilar JF, Alvarado VM, Sandoval Torres CL. Control of the air supply subsystem in a PEMFC with balance of plant simulation. Sustainability 2017;9.